Chemical and photocatalytic oxidative degradation of carbamazepine by using metastable Bi^{3+} self-doped $NaBiO_3$ nanosheets as a bifunctional material

Yaobin Ding[a], Guangli Zhang[a], Xueru Wang[a], Lihua Zhu[b,*], Heqing Tang[a,*]

[a] Key Laboratory of Catalysis and Materials Science of the State Ethnic Affairs Commission and Ministry of Education, College of Resources and Environmental Science, South-Central University for Nationalities, Wuhan 430074, PR China
[b] School of Chemistry and Chemical Engineering, Huazhong University of Science and Technology, Wuhan 430074, PR China

A B S T R A C T

Metastable Bi^{3+} self-doped $NaBiO_3$ (NBO) nanosheets were prepared by using acidic hydrolysis of $NaBiO_3 \cdot 2H_2O$ in HNO_3 solutions. It was found that the as-prepared NBO nanosheets showed both chemical oxidation ability and photocatalytic oxidation activity for the degradation of carbamazepine under visible light irradiation. The pseudo-zero order reaction kinetic constant for the photodegradation of carbamazepine ($20\,mmol\,L^{-1}$) over the metastable NBO nanosheets was $0.087\,min^{-1}$, being 10.4 and 5.0 times that of the photocatalytic oxidation over the stable NBO nanosheets and the chemical oxidation over the metastable NBO nanosheets in dark, respectively. The enhanced photodegradation of carbamazepine over the metastable NBO nanosheets was mainly attributed to a reaction process of photocorrosion of the NBO nanosheets, which increased generation of singlet oxygen from the lattice oxygen of NBO and promoted a synergistic effect between the chemical oxidation and the photocatalytic oxidation. Singlet oxygen and photo-generated holes were identified as the major reactive species for photodegradation of carbamazepine. By a rough estimation, the (dark) chemical oxidation, photocorrosion process and photocatalysis contributed 19.4%, 60% and 20.6% of the total degradation of carbamazepine, respectively. Based on the identification of intermediates by GC– and LC–MS, two degradation pathways of carbamazepine in both chemical oxidation system and photocatalytic system were proposed. The developed dual-reactive-species-based photocatalysis may be a useful technology for the purification of water containing carbamazepine.

© 2016 Elsevier B.V. All rights reserved.

1. Introduction

Pharmaceuticals are a large class of emerging environmental contaminants extensively and increasingly being used in human and veterinary medicine and have received increasing concerns over the last fifteen years. Carbamazepine (CBZ), as an antiepileptic and mood stabilising pharmaceutical, is usually used for the treatment of epilepsy, bipolar disorder and trigeminal neuralgia [1]. Due to its continuous introduction into the environment, low biodegradability and persistent nature in wastewater [2], CBZ has becoming one of the most frequently detected pharmaceuticals in various types of water [3–6], which can affect water quality and potentially impact drinking water supplies, ecosystem and human

health [7]. For example, CBZ has been detected at concentrations of $610\,ng\,L^{-1}$ in groundwater [4] and up to $18\,ng\,L^{-1}$ in drinking water [3], respectively. Moreover, CBZ has been evaluated as toxic to aquatic life including bacteria, algae, invertebrates, and fish [8]. Therefore, there is an urgent need for efficient water treatment technologies for the degradation of CBZ-containing waste-waters.

Photocatalytic technology is known as a promising method because it can mineralize most of organic pollutants through the generation of multiply highly active reactive oxygen species such as photo-generated hole (h^+) and hydroxyl radical ($\bullet OH$) by using solar light irradiation and semiconductor materials [9–11]. Bismuth-based oxides gained much attention due to their excellent photo-activity arising from the exclusive electron structures, and several visible light responsive Bi-containing photocatalysts were reported for the wastewater purification [12,13]. For example, $0.5\,g\,L^{-1}$ hierarchical BiOCl microspheres could almost totally eliminate $2.5\,mg\,L^{-1}$ CBZ after 150 min under the solar light illumination [12]. As bismuth based materials, Bi(V)/Bi(III) mixed

valent oxides have attracted much attention due to their photocatalytic activity and/or chemical oxidation potential. To prepare Bi(V)/Bi(III) mixed valent oxides, two methods were explored as follows. The first one is the oxidation of Bi(III) salts by common oxidants such as persulfate [14] and light triggered photogenerated hole (h^+) [15,16]. Bi_2O_4-decorated BiOBr nanosheets with excellent photocatalytic performance were prepared through a combined action of NaOH-induced dehalogenation and light triggered photogenerated hole (h^+) oxidation processes on the surface of BiOBr nanosheets. The second one is the controllable reduction of sodium bismuthate ($NaBiO_3$) in the acidic solution [17], through ion-exchange with metal ions [18,19] and the hydrothermal treatment [20,21]. Recently, we used inorganic acid to treat $NaBiO_3$ and in-situ and ex-situ prepared metastable Bi(V)/Bi(III) composites, which showed enormously enhanced removal for bisphenol A with singlet oxygen ($^1O_2$) as main reactive species [17,22]. By controlling the concentration of inorganic acid, Bi^{3+} self doped $NaBiO_3$ was prepared via a facile soft-chemical method through the treatment of $NaBiO_3$ nanosheets in the HNO_3 solution and showed much enhanced photocatalytic activity than $NaBiO_3$ nanosheets [23]. Therefore, Bi(V)/Bi(III) mixed valent oxides are anticipated to exhibit simultaneously the chemical oxidation ability and photocatalytic ability for the degradation of organic pollutants under visible-light irradiation. To the best of our knowledge, no investigations have been reported on the use of metastable Bi^{3+} self doped $NaBiO_3$ nanosheets as a bifunctional material for the degradation of organic pollutants such as CBZ.

Herein, metastable Bi^{3+} self doped $NaBiO_3$ (NBO) was prepared with a facile soft-chemical method through a treatment of $NaBiO_3$ nanosheets in HNO_3 solution, and NBO was found to show both chemical oxidation ability and photocatalytic oxidation activity for the efficient degradation of CBZ under visible light irradiation. Under conditions of $1.0\,g\,L^{-1}$ NBO and $20\,\mu mol\,L^{-1}$ CBZ, the visible light photocatalytic oxidation of CBZ achieved a CBZ degradation removal of 99.8% in 60 min, being much higher than that (57%) of the chemical oxidation carried out in dark. The enhanced photodegradation of CBZ over NBO was found to be attributed to a reaction process of photocorrosion of the NBO nanosheets, which increased generation of singlet oxygen from the lattice oxygen of NBO and promoted a synergistic effect between the chemical oxidation and the photocatalytic oxidation. Singlet oxygen and photo-generated holes were identified as the major reactive species for the apparent photocatalytic degradation of CBZ. Based on the identification of intermediates by GC– and LC–MS, we also proposed the photocatalytic degradation pathways of CBZ over metastable NBO.

2. Experimental section

2.1. Materials and chemicals

$NaBiO_3 \cdot 2H_2O$, HNO_3, CBZ, KI, $Na_2S_2O_3$, furfuryl alcohol (FFA), tertbutyl alcohol (TBA), p-benzoquinone (BQ), sodium azide (NaN_3) and triethanolamine (TEA) were provided by Sinopharm Chemical Reagent Co., Ltd. (Shanghai, China). 2,2,6,6-Tetramethylpiperidine (TEMP) was provided by J&K Chemicals (Shanghai, China). All the reagents were of analytical purity and were used as received. Ultrapure water ($18.2\,M\Omega\,cm$) was used for all the experiments.

2.2. Preparation of metastable Bi^{3+} self doped $NaBiO_3$

Metastable NBO nanosheets were prepared by a soft chemical method according to our previous report [23]. Typically, $NaBiO_3 \cdot 2H_2O$ (0.316 g, 1 mmol) was dispersed in 100 mL of double deionized water during stirring. Then, $2\,mmol\,L^{-1}$ HNO_3 solution

was added into the $NaBiO_3$ suspended solutions, the hydrolysis of $NaBiO_3 \cdot 2H_2O$ was started. After 30 min for hydrolysis, the resultant solids were separated, washed with double deionized water and finally dried at 25–100 °C for 8 h, which gave the product of metastable NBO nanosheets. To tune the singlet oxygen generation amount of the prepared samples, different drying temperatures were used, and the resultant samples were denoted as NBO-x, which x represented the drying temperature (°C). In the present work, the molar ratio of $NaBiO_3 \cdot 2H_2O$ to HNO_3 was optimized as 0.2 for the preparation of metastable Bi^{3+} self-doped $NaBiO_3$ nanosheets in the term of the efficient photodegradation of CBZ (Fig. S1).

2.3. Characterization

Powder X-ray diffraction (XRD) was conducted on a Bruker Advanced D8 X-ray diffractometer with Cu K_α radiation, operated at 40 mA and 40 kV. Chemical compositions and valence band spectra were analyzed by X-ray photoelectron spectroscopy (XPS) on a Thermo Escalab 250 XPS instrument with a monochromatic Al K_α X-ray source. All binding energies were referenced to the C 1s peak (284.6 eV) arising from adventitious carbon. The morphology and phase composition of NBO were investigated by scanning electron microscopy (SEM, FEI, the Netherlands) and transmission electron microscopy (TEM, FEI Tecnai G20).

2.4. Chemical oxidation degradation experiments

The chemical oxidation of CBZ over NBO-x nanosheets was conducted without the irradiation of visible light. The experiment was carried out in a 100 mL reactor at 25 °C. NBO-x nanosheets (50 mg) were rapidly dispersed in 50 mL solution of $20\,\mu mol\,L^{-1}$ CBZ to start the degradation experiment. The initial solution pH value was preset at pH 7.2, and the solution pH was not controlled during the degradation process. During the degradation, solution samples (1.0 mL) were taken at given time intervals, quenched immediately by adding $10\,\mu L$ NaN_3 ($1\,mol\,L^{-1}$) and centrifuged at 14,000 rpm for 3 min on an EBA-21 centrifugal (Hettich, Germany) to remove solid particles. The CBZ concentration in the supernatant was determined by high performance liquid chromatography (HPLC), and total organic carbon (TOC) was assayed by using a TOC/TN analyzer. All measurements were repeated three times and the results were reproducible within the experiments errors ($\pm$5%).

Quenching experiments were performed to determine the reactive oxygen species formed in the degradation system by using NaN_3 as a scavenger of $^1O_2$ [24]. The electron spin resonance (ESR) technology was used to confirm the generation of singlet oxygen.

2.5. Photocatalytic oxidation experiments

Photocatalytic oxidation of CBZ was conducted over the NBO-x nanosheets under the illumination of visible-light ($\lambda\pounds\frac{3}{4}420\,nm$). In the experiment, NBO-x nanosheets ($1.0\,g\,L^{-1}$) was added into 50 mL double deionized water containing $20\,\mu mol\,L^{-1}$ CBZ. Then, a 500 W halogen tungsten lamp was turned on, and the photocatalytic degradation of CBZ was started. A 420-nm cutoff was used to ensure the ultraviolet part of illumination was filtered out. At given time intervals, an appropriate amount of the suspension was taken out, and the concentration of residual CBZ was analyzed by using HPLC. All measurements were repeated three times and the results were reproducible within the experiments errors ($\pm$5%).

The photocurrent was measured on a CHI660 electrochemical workstation (Chenghua, Shanghai) in the electrolyte solution of 0.5 M Na_2SO_4 at a bias potential of 0.1 V under the irradiation of a 300 W xenon lamp with a 420-nm cutoff. The measurement was conducted in a standard three-electrode cell with a working
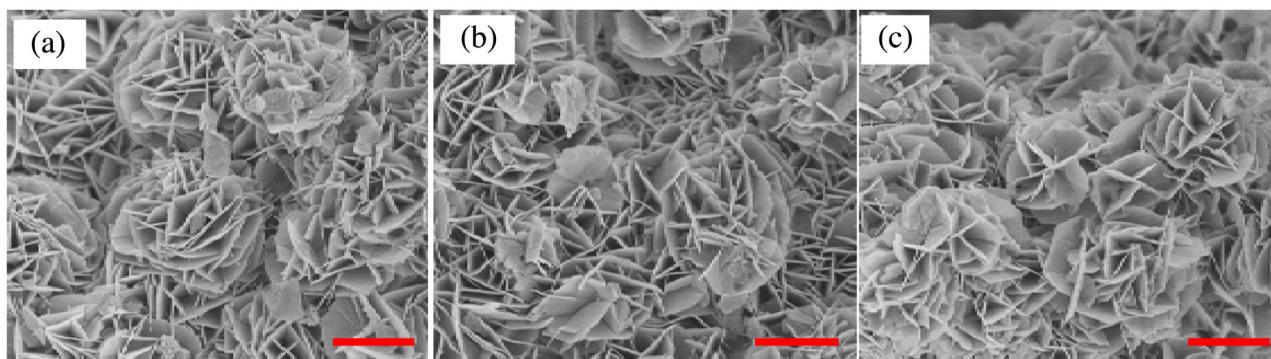
Fig. 1. SEM images of (a) NaBiO$_3$, (b) NBO-25 and (c) NBO-100. Scale bars are 1 μm.

electrode (as-prepared NBO-x nanosheets), a platinum sheet as auxiliary electrode, and a standard calomel electrode (SCE) as reference electrode. The working electrode was fabricated as follows. NBO-x nanosheets (20 mg) were dispersed in 5 mL ethanol, and the obtained slurry was then dip-coated onto the surface of a conductive glass electrode (ITO) with a circular exposure area (d = 3.5 mm). After being dried at 25 °C for 8 h, the coated ITO electrode was used as the working electrode.

To identify the active species in the photocatalytic process, TEA and NaN$_3$ were added into the CBZ degradation system as a quencher of holes (h$^+$) and ^{1}O$_2$, respectively [24,25].

2.6. Chemical analysis

The concentration of residual CBZ in degradation solution was analyzed on a HPLC (Agilent 1200 infinity series) with a G1315D 12600 DAD detector at a wavelength of 210 nm. An amethyst C18-P column (5 μm, 4.6 × 150 mm) was used as separation column and a mixture of methanol and water (55: 45, v/v) was used as the mobile phase with a flow rate of 0.8 mL min^{-1} for HPLC experiments. The injection volume was 50 μL.

For the identification of degradation intermediates and products, solution samples (2.0 mL) were taken after 10 min in the photocatalytic system and 60 min in the chemical oxidation system, respectively. The degradation intermediate products of CBZ were monitored by the mass spectrometer (Agilent 1100 LC/MSD Trap, USA) in electrospray positive ion (ESI$^+$) mode with methanol and water (55: 45, v/v) as the mobile phase with a flow rate of 0.8 mL min^{-1} and the injection volume of 50 μL.

The degradation intermediates of CBZ were also analyzed by GC–MS on a Thermo scientific TRACE 1300 GC Ultra system with the electron ionization mode. A TR-35MS capillary column (30 m × 0.25 mm × 0.25 μm) was used for analysis. Prior to GC–MS analysis, the supernatant (40 mL) was extracted with dichloromethane (5 mL × 3). The organic extracts were dried over anhydrous Na$_2$SO$_4$ and concentrated to 1 mL by rotary evaporation. The initial temperature of the column oven was hold at 60 °C for 1 min, and then increased to 280 °C with a heating rate of 6 °C min^{-1}. Helium was used as the carrier gas. Mass spectrometric detection was operated with 70 eV electron impact (EI) mode at an ionization current of 50 μA and an ion source temperature of 250 °C. The mass spectra were recorded in full scan mode (m/z 50–600) for qualitative analysis.

The concentration of FFA was determined by HPLC on a Thermo scientific DIONEX UltiMate-3000 HPLC system under following conditions: column, RP-C18 (5 μm, 4.6 × 150 mm); mobile phase, 40/60 (MeOH/H$_2$O) at a flow rate of 0.9 mL min^{-1}; detector, DAD detector at 219 nm.

Total organic carbon (TOC) was assayed by using TOC analyzer micro N/C model (Analytik Jena, Germany).

The total amount of Bi in the bulk NaBiO$_3$ nanosheets and metastable Bi^{3+} self-doped NaBiO$_3$ nanosheets was measured by inductively coupled plasma-atomic emission spectroscopy (ICP-AES) after dissolving the sample with 1 mol L^{-1} HNO$_3$. The amount of Bi(V) in the bulk NaBiO$_3$ and metastable Bi^{3+} self-doped NaBiO$_3$ nanosheets was determined by iodometry. For the determination, the samples (200 mg) were added into 50 mL of 1 mol L^{-1} HNO$_3$ containing 0.2 mol L^{-1} KI. After reacted for 1 h, the generated I$_2$ was measured through titration by using 0.1 M Na$_2$S$_2$O$_3$ as the titrant and 1% starch solution as the indicator [21]. Based on the analysis above, the atomic percentage of Bi^{3+} in the total Bi of the bulk NaBiO$_3$ and NBO-x samples were calculated (Bi^{3+} + Bi^{5+}).

3. Results and discussion

3.1. Characterization of catalysts

As shown in Fig. 1a, NaBiO$_3$·2H$_2$O presented a typical flake morphology, composed of nanosheets with width (length) of ~1.0 μm and thickness of 10–15 nm. Both NBO-25 and NBO-100 samples showed little change in the morphology as compared with NaBiO$_3$·2H$_2$O as shown in Fig. 1b and c.

The as-prepared NBO-x samples were further characterized by XRD and XPS analysis. As shown in Fig. 2a, the NBO-x samples dried at different temperatures presented typical diffraction peaks of NaBiO$_3$·2H$_2$O at 2θ = 11.5°, 18.3°, 28.6°, 32°, 33.1°, 47.6°, and 56.6° (JCPDS30-1161, space group R3, with lattice parameters a = 5.564°A, c = 15.99°A, ρ = 120°), indicating that the crystal structure of NBO samples had no obvious change compared with that of NaBiO$_3$·2H$_2$O [18,23]. XPS Bi 4f (4f 5/2 and 4f 7/2) envelops of NaBiO$_3$·2H$_2$O, NBO-25 and NBO-100 were given in Fig. 2b. As we know, the Bi 4f 5/2 and Bi 4f 7/2 peaks of NaBiO$_3$·2H$_2$O observed at 164.5 eV and 159.4 eV were assigned to Bi^{5+} species on the surface. After acidic hydrolysis of NaBiO$_3$·2H$_2$O, the Bi 4f peaks of NBO samples became asymmetric with sub-peaks occurred at lower binding energies, suggesting that Bi^{3+} was formed on the surface of NBO. According to the deconvoluted spectra, the atomic percentages of Bi^{3+} and Bi^{5+} on surface of NBO-25 and NBO-100 were estimated. The percentage of Bi^{5+} and Bi^{3+} on NBO-25 surface was 65.5% and 34.5%, respectively. Moreover, the drying at higher temperatures such as 100 °C did not change the Bi species on the surface of NBO. As shown in Fig. 2c, the O1s XPS envelops of NaBiO$_3$·2H$_2$O, NBO-25 and NBO-100 could be deconvoluted into three peaks at binding energies of 529.5, 531.2, and 533.2 eV, corresponding to the lattice oxygen (Bi—O), chemisorbed oxygen and physically adsorbed oxygen, respectively. Compared with NBO-25, the atomic percentage of the lattice oxygen (Bi—O) on the surface of NBO-100 was
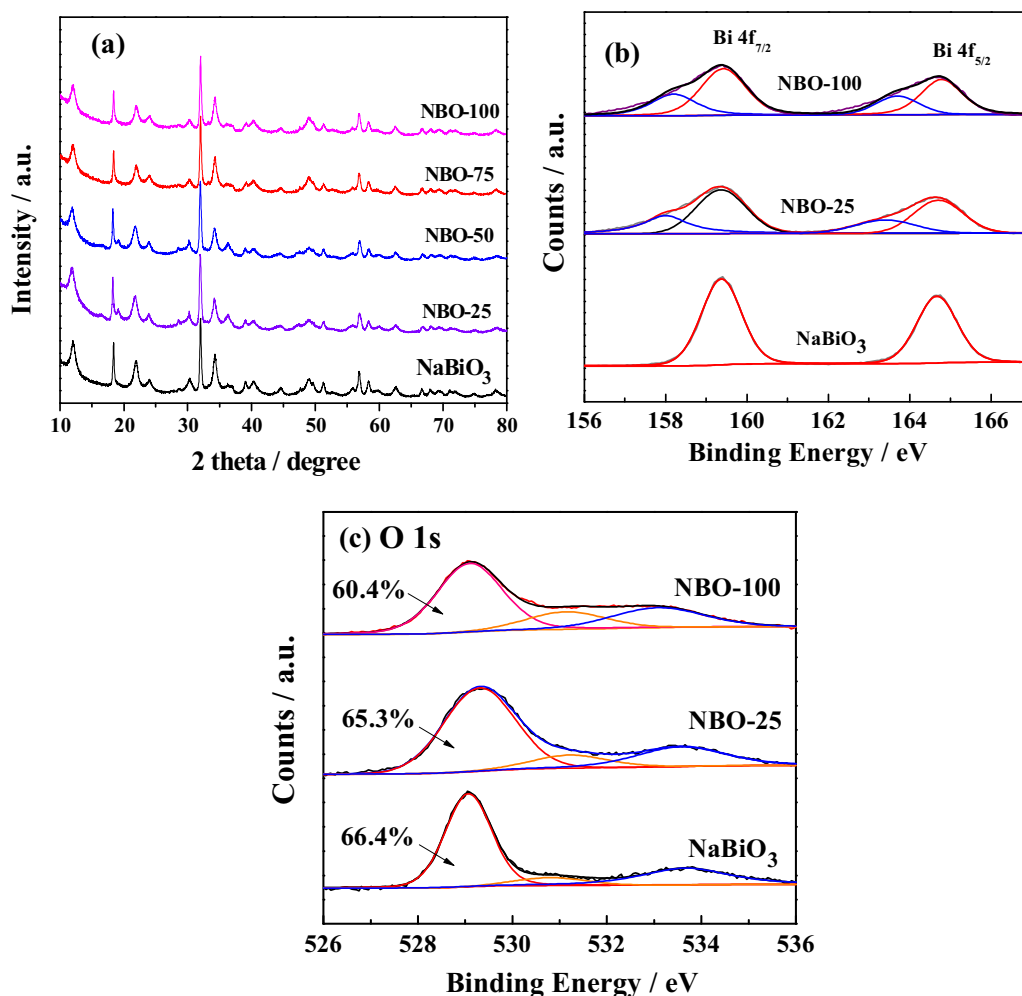
Fig. 2. (a) XRD patterns of NaBiO$_3$ and NBO-x samples. (b,c) High-resolution XPS spectra of NaBiO$_3$, NBO-25 and NBO-100: Bi 4f (b) and O 1s (c).

decreased to 60.9% from 65.8%, indicating that the as-prepared NBO-25 was instable and the drying treatment induced a release of instable lattice oxygen. The doping of Bi^{3+} in the bulk NBO-x samples was further confirmed by the determination of Bi^{3+} content. For NaBiO$_3 \cdot 2H_2O$, no Bi^{3+} was detected, being in good agreement with the XPS result as shown in Fig. 2b. The atomic percentage of Bi^{3+} in total Bi (Bi^{3+} + Bi^{5+}) was 8.7% and 8.8% in the bulk NBO-25 and NBO-100 samples, respectively (Table S1). The lower atomic percentage of Bi^{3+} in total Bi of the bulk sample in comparison with that on its surface (34.5%) suggests that the hydrolysis of NaBiO$_3 \cdot 2H_2O$ in HNO$_3$ was an interface controlled reaction. Both the increased atomic percentages of Bi^{3+} in the bulk sample and on the surface of the catalysts clearly demonstrated that the acidic treatment induced the reduction of Bi^{5+} to Bi^{3+} in the NaBiO$_3$ lattice and the formation of Bi^{3+} self doped NaBiO$_3$ nanosheets.

The UV–vis DRS spectra of NaBiO$_3$, NBO-25 and NBO-100 samples were listed in Fig. 3. It can be clearly seen that compared to NaBiO$_3$, NBO-25 and NBO-100 samples showed much stronger absorption in the visible light region. The enhanced absorption in the visible light region was suggested to be attributed to the O defect existed in the crystal structure of NBO-25 due to the formation of Bi^{3+} upon the treatment in the HNO$_3$ solution. The drying treatment at 100 °C induced the formation of more O defect due to the release of lattice oxygen. Therefore, the absorption intensity of NBO-100 was obviously higher than that of NBO-25 in the visible region. The upper right inset in Fig. 3 showed the pictures of the corresponding products with different colors. The main absorption
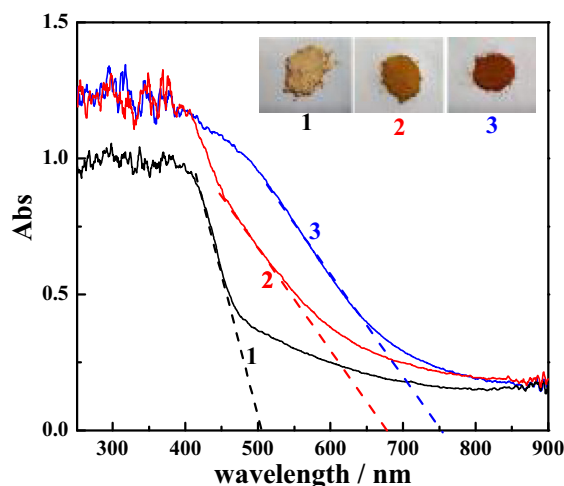

Fig. 3. UV–vis DRS spectra of (1) NaBiO$_3 \cdot 2H_2O$, (2) NBO-25 and (3) NBO-100.

edge (λ_g) for NaBiO$_3$, NBO-25 and NBO-100 samples was estimated to be about 50 nm, 667 nm and 740 nm, corresponding to the band gap energy of 2.45 eV, 1.83 eV and 1.68 eV, respectively.
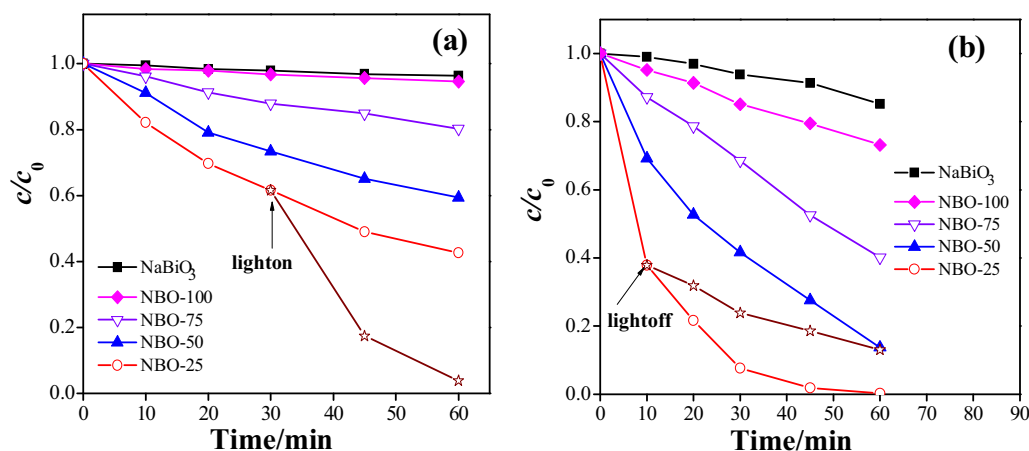
Fig. 4. Effect of drying temperature on the (a) chemical oxidation and (b) photocatalytic oxidation of CBZ (20 μmol L⁻¹) over different catalysts (1.0 g L⁻¹) of metastable Bi³⁺ self doped NaBiO₃ (NBO-x) and NaBiO₃ nanosheets.

3.2. Dark chemical oxidation and photocatalytic oxidation of CBZ by NBO

The chemical oxidation of CBZ by NBO-x nanosheets as a source of singlet oxygen under dark conditions was investigated as shown in Fig. 4a. It was observed that the higher drying temperature caused a depression of the CBZ degradation by NBO-x. For example, the CBZ removal in 60 min was decreased from 57% for the drying treatment at 25 °C to only 6% at 100 °C. Similar to dark oxidation of CBZ by NBO-x, the drying temperature greatly affected the visible light driven photocatalytic oxidation of CBZ over NBO-x. For instance, the photocatalytic removal of CBZ in 60 min was increased from 27% at a drying temperature of 25 °C (NBO-100) to almost 100% at 100 °C (NBO-25). Therefore, it can be concluded that a lower drying temperature facilitates both the chemical catalytic and photocatalytic activity of NBO toward the degradation of CBZ, which may be mainly attributed to the higher chemical oxidation capability of NBO-x dried at lower drying temperatures (Fig. 4a).

To further investigate the role of visible light illumination in the photocatalytic oxidation process of CBZ with NBO-x samples as a bifunctional material, the removal of CBZ was compared between the switching on and off of visible light illumination. As shown in Fig. 4a, during the chemical oxidation process, the removal of CBZ in 30 min was 38%. At reaction time of 30 min, visible light illumination was switched on. The degradation of CBZ in 60 min was elevated to 96%, much higher than that (57%) in the single chemical oxidation process. Instead by the switching off visible light illumination at 10 min in the photocatalytic oxidation process, the degradation of CBZ in 60 min was decreased from 99.8% for the photocatalytic oxidation system to 87%. Therefore, it was concluded that visible light illumination had great influence on the removal of CBZ in the photocatalytic oxidation process with NBO-x samples as a bifunctional material.

Considering the chemical oxidation ability of NBO-100 was almost completely deactivated (the generation amount of ¹O₂ was only 0.7% of that induced by NBO-25 as observed in Fig. 5a), NBO-100 samples were used as a representative of the inherent photocatalytic ability of NBO-x samples. The pseudo-zero order reaction kinetic constant for the photodegradation of CBZ (20 μmol L⁻¹) over the metastable NBO-25 nanosheets was 0.087 min⁻¹, being 10.4 and 5.0 times that of the photocatalytic oxidation over the stable NBO nanosheets and the chemical oxidation over the metastable NBO nanosheets in dark, respectively. Furthermore, the synergistic effect of chemical oxidation and photocatalytic oxidation during the NBO-x photocatalytic process was
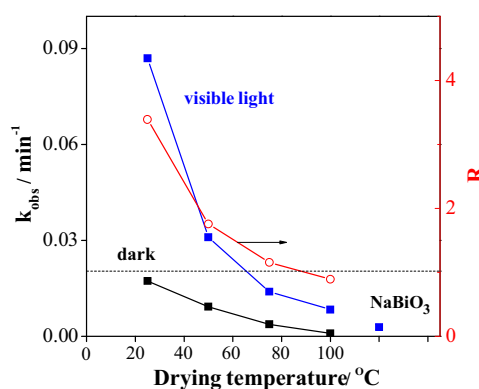

Fig. 5. (a) Amount of $^1O_2$ generated from NBO-x (x = 25, 50, 75, 100) in aqueous solutions. (b) A correlation of degradation constant of CBZ in the chemical oxidation system with the amount of $^1O_2$ generated from NBO-x (x = 25, 50, 75, 100) in aqueous solutions.

evaluated. For this purpose, R value was defined as the ratio of $k_{obs,photo}$ to the sum of $k_{obs,chem}$ and $k_{obs,photo}^{NBO-100}$ as described in Eq. (1).

$$R = \frac{k_{obs,\, photo}}{k_{obs,\, chem} + k_{obs,\, photo}^{NBO-100}} \tag{1}$$

where $k_{obs,photo}$ is the pseudo-first-order rate constant for the photocatalytic system, $k_{obs,chem}$ is the pseudo-first-order rate constant for the chemical oxidation system and $k_{obs,\, photo}^{NBO-100}$ is the pseudo-first-order rate constant for the photocatalytic system ($k_{obs,photo}$) with NBO-100 as an assumed "pure" photocatalyst.

As shown in Fig. 6, the apparent pseudo-first-order rate constant ($k_{obs,}$ i.e., $k_{obs,chem}$ or $k_{obs,photo}$) was obtained by fitting the experimental data to Eq. (2).

$$-\frac{d[CBZ]}{dt} = k_{obs}[CBZ] \tag{2}$$

Through the calculation, it was found that when the drying temperature was lower than 100 °C (i.e., except of NBO-100), all the NBO-x samples (x = 25, 50 and 75) gave a R value of more than 1, indicating that these NBO samples functioned as bifunctional materials and there is synergistic effect between chemical oxidation and photocatalytic oxidation during the photocatalytic process.
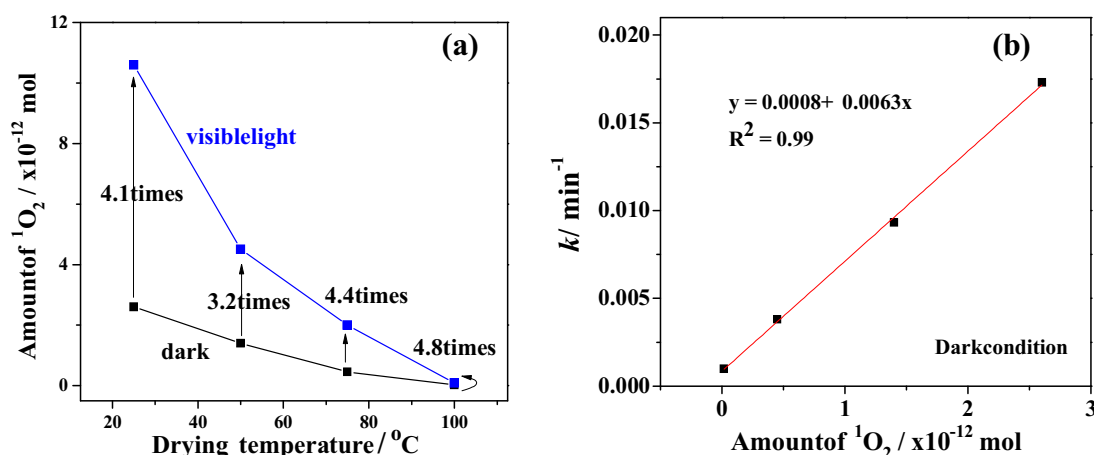
Fig. 6. Apparent pseudo-first-order rate constant (k_{obs}) of the CBZ degradation in the chemical oxidation and photocatalytic oxidation systems.

3.3. Mineralization of CBZ by NBO

The mineralization of CBZ in the two systems was investigated to further evaluate the higher photocatalytic oxidation activity of metastable NBO nanosheets as compared to its chemical oxidation ability (Fig. S2). When NBO-25 was used, after 120 min reaction, about 78% of TOC removal was observed in the photocatalytic system, being much higher than 23% TOC removal in the chemical oxidation system (Fig. S2a). This further demonstrated the advantage of the photocatalytic system on the degradation and mineralization of CBZ. The same enhanced effect on CBZ mineralization was also observed with other NBO-x samples in the photocatalytic system (Fig. S2b).

3.4. Identification of mainly reactive species

In our previously reported work, dark chemical oxidation by inorganic acid treated $NaBiO_3$, singlet oxygen was identified as the key role in the organic pollutants degradation [17]. The reactive oxygen radicals in the chemical oxidation processes over NBO-25 as an example were identified by using radical scavenging techniques. It was observed that the addition of 100 mmol L^{-1} NaN_3 almost completely depressed the CBZ degradation (Fig. S3a), indicating that singlet oxygen was mainly responsible for the CBZ degradation. ESR measurements also clearly indicated the generation of singlet oxygen in this system (Fig. S3b).

The amount of $^1O_2$ generated from NBO-x (x = 25, 50, 75, 100 °C) in the reaction solution was measured using FFA as a probe. As illustrated in Fig. 5a, increasing the drying temperature obviously decreased the amount of $^1O_2$ generated from NBO-x samples. Moreover, a linear correlation of the pseudo-first-order rate constant for the chemical oxidation system ($k_{obs,chem}$) with the amount of $^1O_2$ generated from NBO was observed as shown in Fig. 5b. These results all demonstrated that $^1O_2$ generated from NBO-x was reactive oxygen species responsible for the degradation of CBZ in the chemical oxidation system.

Compared to the dark chemical oxidation reaction, in the photocatalytic system, adding 100 mmol L^{-1} NaN_3 also caused the obvious decrease of CBZ degradation, but it could not completely depress the photocatalytic degradation of CBZ over NBO-25. This indicated that $^1O_2$ was involved in the CBZ degradation as main reactive oxygen species, but there were also other species responsible for the CBZ degradation in the photocatalytic system. In our previous work, photo-generated holes were identified as the key reactive species in the photocatalytic Bi^{3+} self doped $NaBiO_3$ system [23]. TEA was used here as a scavenger of photo-generated

holes to study its role in the CBZ degradation. As demonstrated in Fig. 7a, adding 20 mmol L^{-1} TEA significantly depressed the photocatalytic degradation of CBZ over NBO-25 and a CBZ degradation removal of 77% was observed in 60 min, suggesting the involvement of photo-generated holes as a reactive species in the CBZ degradation. Moreover, the simultaneous addition of 20 mmol L^{-1} TEA and 100 mmol L^{-1} NaN_3 dropped the CBZ removal to only 5% in 60 min. Therefore, both photo-generated holes and $^1O_2$ were identified as the key reactive species for CBZ degradation in the photocatalytic system.

The effect of drying temperature on the accumulation of the photo-generated holes and $^1O_2$ in the photocatalytic NBO-x systems was investigated in detail by using radical scavenging techniques. As clearly shown in Fig. 7b, for the drying temperature of 100 °C, the CBZ removal in 60 min was 27%, which was mainly caused by the generated holes. When the drying temperature was decreased, the amount of singlet oxygen generated from NBO-x was accordingly increased, resulting in the increased contribution of singlet oxygen to the overall degradation of CBZ. For the drying temperature of 25 °C, the generated singlet oxygen resulted in a CBZ removal of 77% in 60 min. On the other hand, the photo-generated holes contributed a CBZ degradation of 21% in 60 min.

Moreover, the effect of the illumination of visible light on the generation amount of singlet oxygen was investigated. As shown in Fig. 5a, the illumination of visible light enhanced the generation of $^1O_2$ in the photocatalytic NBO-x system. For NBO-25, the amount of generated $^1O_2$ under the illumination of visible light was measured to be 1.06×10^{-11} mol, being 4.1 times that without the illumination of visible light. For almost completely deactivated NBO-100 samples, the illumination of visible light increased the amount of generated $^1O_2$ by 3.8 times. In the photocatalytic system, $^1O_2$ can be generated from the reaction of dissolved oxygen with photo-generated electrons and holes [26,27]. Therefore, decreasing the concentration of dissolved oxygen in the reaction solution could obviously depress the amount of generated $^1O_2$ and the degradation of CBZ. However, as shown in Fig. 7a, the CBZ degradation in the photocatalytic system was not obviously decreased by the bubbling of N_2. These results indicated that the enhanced generation of $^1O_2$ was not from the activation of dissolved oxygen. The enhanced generation of $^1O_2$ under the illumination of visible light could be attributed to the release of weakly bonded lattice oxygen through the photocorrosion process, which was widely observed with ZnO based photocatalytic systems [28,29].

Based on discussion above, the degradation of CBZ under the illumination of visible light was attributed to the contribution of three reaction processes (dark chemical oxidation, photocor-
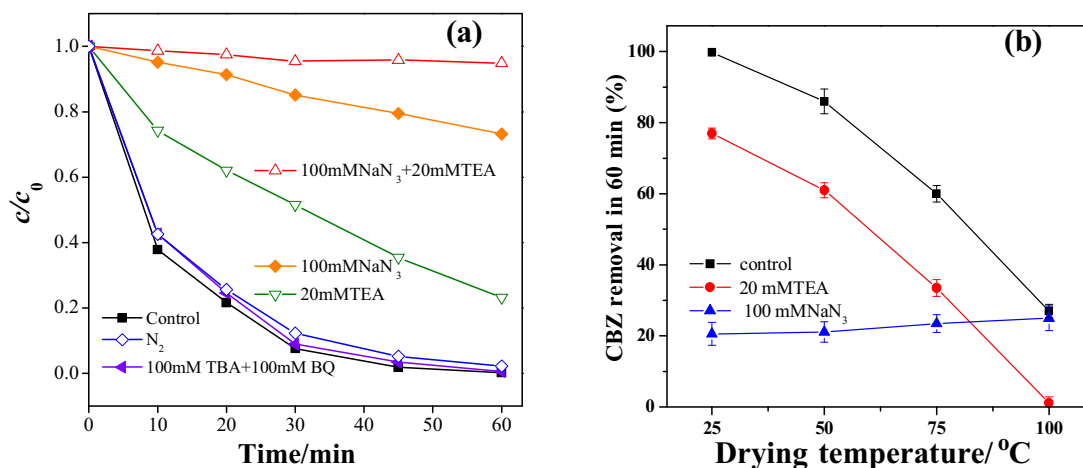
Fig. 7. (a) Effect of radical quenchers on the photocatalytic degradation of CBZ over NBO-25 samples under visible light irradiation. (b) Effect of radical quenchers on the photocatalytic degradation removal (in 60 min) of CBZ over NBO-x samples under visible light irradiation.
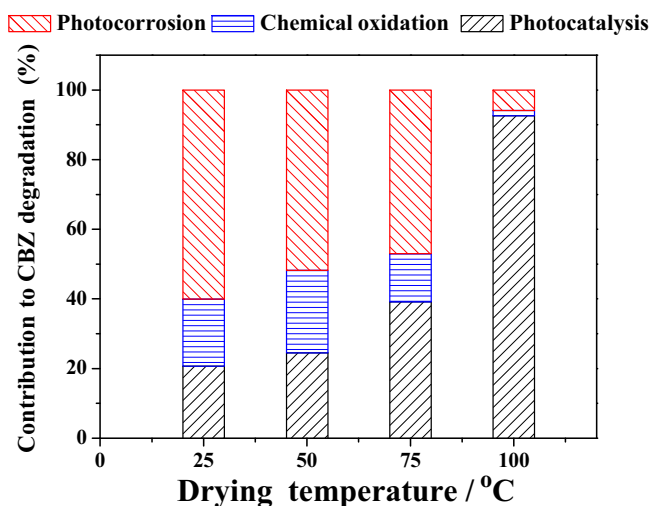

Fig. 8. Contributions of dark chemical oxidation, photocorrosion and photocatalysis to the degradation of CBZ over NBO-x samples under visible light irradiation.

rosion and photocatalysis). Based on the measured amount of generated $^1O_2$, the contribution of three reaction processes to the degradation of CBZ under the illumination of visible light was further evaluated. For NBO-25, the amount of generated $^1O_2$ under the illumination of visible light was 4.1 times that without the illumination of visible light. Therefore, the contribution of photocorrosion to the overall amount of generated $^1O_2$ was calculated as 80.4% ($(4.1 - 1)/4.1 \times 100\% = 75.6\%$). By a rough estimation, the dark chemical oxidation, photocorrosion and photocatalysis contributed 19.4%, 60% and 20.6% to the total degradation of CBZ, respectively (Fig. 8).

3.5. Evolution of NBO-25 nanosheets during degradation process

To investigate evolution of NBO-25 during the chemical oxidation and photocatalytic oxidation processes, the recycling and reusability of NBO-25 were conducted (Fig. S4). As an oxidant, NBO-25 was consumed during the dark degradation of CBZ, which resulted in the gradual decrease of its chemical oxidation reactivity in the sequent three runs (Fig. S4a). This "consumption" of the chemical oxidation reactivity of NBO-25 also induced remarkably declining of the photodegradation of CBZ (Fig. S4b). However, it should be noted that the consumption of chemical oxidation ability

during the photodegradation process did not decrease the "inherent" photocatalytic activity of metastable Bi^{3+} self-doped $NaBiO_3$ nanosheets (obtained with the addition of 100 mmol L^{-1} NaN_3). Even after the complete consumption of chemical oxidation ability, the catalyst can further photocatalytically degrade CBZ (Fig. S4b).

To clarify the varied degradation of CBZ in the chemical oxidation and photocatalytic systems over NBO-25, the morphology, structure and surface properties of NBO-25 nanosheets during the chemical oxidation and photocatalytic oxidation process were tracked by SEM, XRD and XPS analysis. As shown in Fig. 9a, after the chemical oxidation of CBZ in the first run, the recycled samples still kept nanosheet in the morphology as compared with NBO-25 (Figs. 1 b and 9 a). However, after four runs of the degradation, the nanosheet structure of the used samples was partly destroyed (yellow arrows in Fig. 9b). Moreover, as clearly shown in Fig. 9c and d, the illumination of visible light intensified the destruction of nanosheet structure of the used samples during the photocatalytic oxidation process.

The XRD patterns of the used NBO-25 samples after the photocatalytic degradation and singlet oxygen oxidation of CBZ were shown in Fig. 10a. For the used samples after 4 cycles during chemical oxidation, the characteristic peak at $2\theta = 11.9°$ assigned to the perovskite-like structure of $NaBiO_3 \cdot 2H_2O$ became weak, indicating a part decomposition of the crystal structure of NBO-25. For the used samples after 4 recycles during photocatalytic degradation, the peak intensity was much weaker as compared with that of the used samples during chemical oxidation, suggesting that the illumination of visible light intensified the destruction of the crystal structure of NBO-25.

The reduction of lattice oxygen in the crystal structure of NBO-25 was further confirmed by the XPS O1s spectra of used NBO-25 samples after the chemical oxidation and photocatalytic degradation experiments. As illustrated in Fig. 10b, the O1s XPS envelops of fresh and used $NaBiO_3 \cdot 2H_2O$ could be deconvoluted into three different peaks at binding energies of 529.5, 531.2, and 533.2 eV, corresponding to the lattice oxygen (Bi—O), chemisorbed oxygen and physically adsorbed oxygen, respectively. The atomic percentage of the lattice oxygen (Bi—O) was 65.3% for fresh NBO-25, which was decreased to 61.5% and 48.3% for the used NBO-25 samples after the chemical oxidation and photocatalytic degradation experiments, respectively. These results indicated that lattice oxygen in the crystal structure of NBO-25 samples was consumed for the degradation of CBZ, and the illumination of visible light enhanced the photocorrosion of NBO-25 samples by promoting the release of lattice oxygen in the form of singlet oxygen.
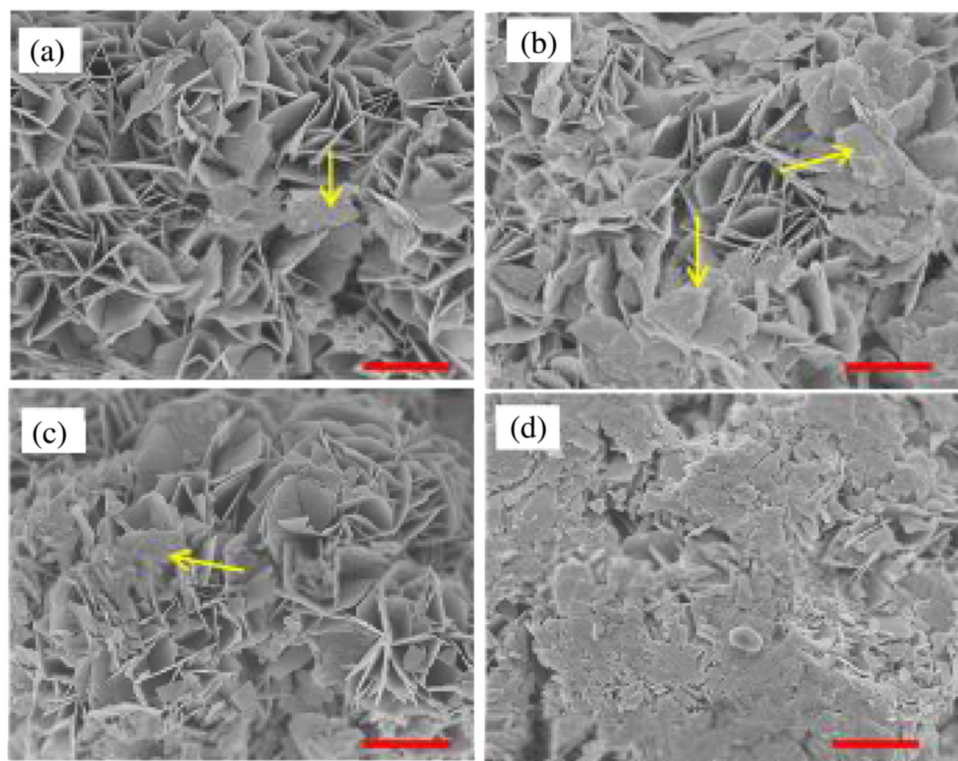
Fig. 9. SEM images of used NBO-25 samples after (a, c) 1 run and (b, d) 4 runs during (a, b) chemical oxidation and (c, d) photocatalytic oxidation processes. Scale bars are 1 μm.
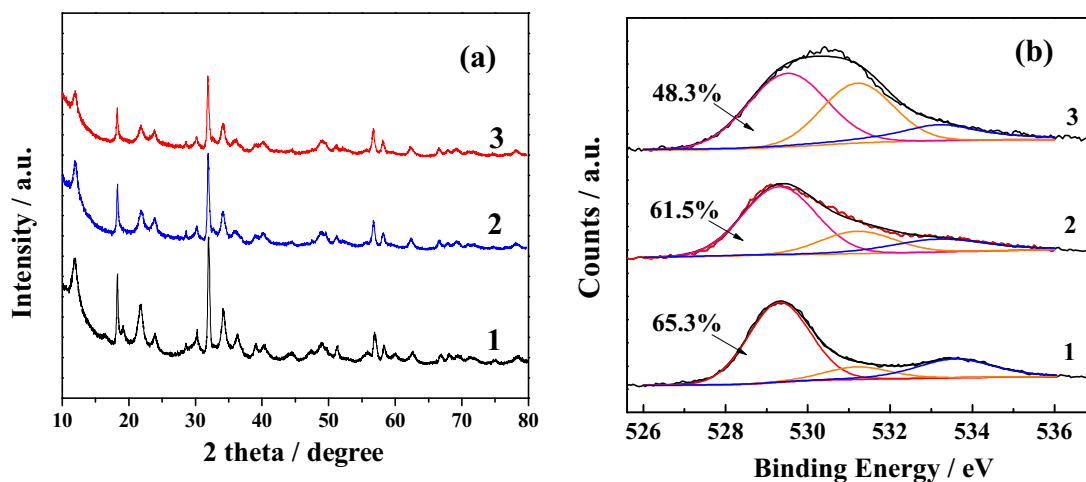

Fig. 10. (a) XRD patterns and (b) XPS O1s spectra of (1) fresh NBO-25, and the reused NBO-25 after (2) the chemical oxidation and (3) the photocatalytic degradation being carried out for 4 runs.

3.6. Mechanism for the enhanced photocatalysis of metastable Bi^{3+} self doped $NaBiO_3$

As discussed above, the photodegradation of CBZ over metastable Bi^{3+} self doped $NaBiO_3$ under the illumination of visible light was attributed to the three reaction processes: the chemical oxidation, photocatalysis and photocorrosion. Therefore, the reaction mechanism for photodegradation of CBZ over metastable Bi^{3+} self doped $NaBiO_3$ was discussed in three parts.

Firstly, in the chemical oxidation process, the chemical oxidation of metastable Bi^{3+} self-doped $NaBiO_3$ is originated from its contained Bi(V) oxidation state. $NaBiO_3 \cdot 2H_2O$ crystals show relative chemical and crystal stability in the aqueous solution with pH

values higher than pH 9 [22]. However, when $NaBiO_3 \cdot 2H_2O$ crystals were suspended in acidic solutions, its crystal structure will be destroyed through a hydrolysis reaction, leading to the formation of Bi^{3+} defects. As a result, part lattice oxygen is released in the form of O_2 in order to keep the charge neutrality in the lattices during the preparation of NBO-25 as confirmed by XPS analysis (Fig. 2c) according to Reaction (3) [17,18].

$$2Bi^{5+} + 6O^{2-} \rightarrow Bi^{3+} + Bi^{5+} + O_{vac} + 0.5O_2 + 5*O^{2-} \qquad (3)$$
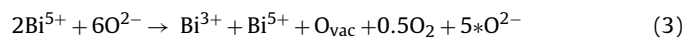
where O_{vac} and $*O^{2-}$ stand for oxygen vacancy and weakly bonded lattice oxygen, respectively. When NBO-25 is used for the degradation of CBZ in dark, part weakly bonded $*O^{2-}$ ions is released in the
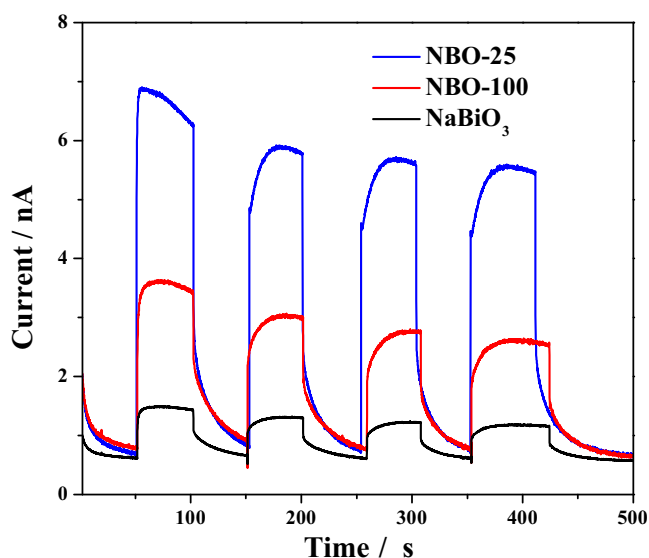
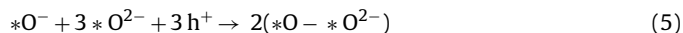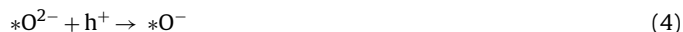**Fig. 11.** Photocurrents of NBO-25, NBO-100 and $NaBiO_3 \cdot 2H_2O$.

form of $^1O_2$ ($2Bi^{5+} + 2^*O^{2-} \rightarrow 2Bi^{3+} + ^1O_2$), inducing the degradation of CBZ.

For the inherent photocatalysis process of NBO-25 (obtained with the addition of $100\,mmol\,L^{-1}$ NaN_3), as shown in Fig. 7a, the pseudo-first-order rate constant for the photocatalytic degradation of CBZ over stable NBO-25 is $5.2 \times 10^{-3}\,min^{-1}$, being 2.0 times that over $NaBiO_3$ nanosheets. In agreement with our previous report [23], the enhanced catalytic photocatalytic performance of Bi^{3+} self doped $NaBiO_3$ nanosheets induced by Bi^{3+} doping is attributed to the increased visible light adsorption (Fig. 3) and enhanced separation of photogenerated electron-hole pairs (Fig. 11).

For the photocorrosion process, singlet oxygen was confirmed to be generated from the release of more relatively weakly bonded lattice oxygen from the NBO-25 induced by the illumination of visible light based on the following three points. (1) As shown in Fig. 7a, CBZ degradation in the photocatalytic system was not obviously decreased by the bubbling of N_2, indicating that the enhanced generation of $^1O_2$ was not from the activation of dissolved oxygen. (2) Molar ratio of $NaBiO_3 \cdot 2H_2O$ to HNO_3 and drying temperature had great influences on the generation of $^1O_2$ in the photocatalytic system (Fig. S1b and Fig. 5a). During the preparation process of NBO nanosheets, when excess HNO_3 was used to treat $NaBiO_3 \cdot 2H_2O$, more lattice oxygen in $NaBiO_3$ was released during the hydrolysis process, which inevitably decreased the amount of weakly bonded O^{2-} ions and the amount of Bi(V) in the treated $NaBiO_3$ (Figs. S5 and S6). During the drying process of NBO nanosheets at high temperatures, part weakly bonded O^{2-} ions of NBO-25 were pre-released (Fig. 3c). Therefore, the amount of singlet oxygen generated from the NBO-25 was decreased through the photocorrosion process. (3) The atomic percentage of the lattice oxygen (Bi—O) was decreased from 65.3% for fresh NBO-25 to 48.3% for the used NBO-25 samples after the photocatalytic degradation experiments (Fig. 10b). SEM and XRD analysis also suggested that the illumination of visible light intensified the photocorrosion of the crystal structure of NBO-25. Based on these results, it can be concluded that the enhanced amount of singlet oxygen in the photocatalytic system is generated from NBO-25 through the photocorrosion process.

To further get an insight on the generation process of singlet oxygen from the NBO-25 induced by the illumination of visible light, we measured the photocurrents produced by NBO-25 with NBO-100 as control. As shown in Fig. 11, the photocurrent produced by NBO-25 under the illumination of visible light was about 5.7 nA,

being 1.9 times that produced on NBO-100. This result indicates that the photo-generated h^+-e^- pairs in NBO-25 nanosheets can be more efficiently separated than that in NBO-100 nanosheets. The efficient separation of the photo-generated h^+-e^- pairs was attributed to the trap of photo-generated h^+ by the weakly bonded oxygen ($^*O^{2-}$) in the NBO-25 crystals, being similar to the previously reported photocorrosion of ZnO photocatalysts [28,29]. The photocorrosion process can be described as follows,

$$*O^{2-} + h^+ \rightarrow *O^- \tag{4}$$

$$*O^- + 3*O^{2-} + 3h^+ \rightarrow 2(*O - *O^{2-}) \tag{5}$$

$$(*O - *O^{2-}) + 2h^+ \rightarrow {}^1O_2 \tag{6}$$

Therefore, in the photocorrosion process, photo-generated h^+ was trapped by the weakly bonded oxygen ($^*O^{2-}$) instead of its recombination with photo-generated e^-. As a result, an enhanced photocurrent and generation of singlet oxygen from NBO-25 nanosheets was observed under the illumination of visible light.

Moreover, in the photocorrosion process of NBO-25, the release of weakly bonded lattice oxygen induced the doping of Bi-O_{vac} in the NBO crystals and the production of byproduct photocatalysts with the higher photocatalytic activity in comparison with $NaBiO_3 \cdot 2H_2O$. As shown in Fig. S4b, the consumption of chemical oxidation ability through the release of weakly bonded lattice oxygen during the degradation process did not decrease the inherent photocatalytic activity of NBO-25. In each of the four runs, the pseudo-first-order rate constant for the photocatalytic degradation of CBZ over NBO-25 was about $5.2 \times 10^{-3}\,min^{-1}$ (obtained with the addition of $100\,mmol\,L^{-1}$ NaN_3), being 2.0 times that over $NaBiO_3 \cdot 2H_2O$ nanosheets.

Based on the above discussion, the much enhanced photodegradation of CBZ by using metastable Bi^{3+} self-doped $NaBiO_3$ nanosheets is attributed to the combination effect of three processes of the chemical oxidation, photocorrosion and photocatalysis.

3.7. Identification and evolution of degradation intermediates

Time course profiles of HPLC spectra were recorded during the CBZ degradation by NBO-25 in the photocatalytic system and the chemical oxidation system (Fig. S7). The peak area of CBZ was gradually decreased with the reaction time in the both systems, accompanied by simultaneously appearing of several new characteristic peaks, which confirmed the efficient removal of CBZ and the formation of degradation intermediates. All degradation intermediates were eluted at lesser retention time because these intermediates are more polar than CBZ.

Through LC–MS analysis, thirteen CBZ degradation intermediates were detected similarly in the chemical oxidation process and the photocatalytic oxidation process (Table S2 and Fig. S8). Possible chemical structures of each intermediate were proposed according to the molecular ion masses, MS2 fragmentation patterns (MS2 spectra for each intermediate were provided in the Supporting information), and the information available from previous studies (Fig. S8). It was observed that the MS spectrum showed $[M+H]^+$ molecular ion peak at m/z 236.8 with the retention time of 12.6 min, which was attributed to the parent compound of CBZ in accordance with the formula of $C_{15}H_{12}N_2O$ (M = 236). The intermediate P7 showed a molecular ion at m/z 253.0 ($[M+H]^+$ $C_{15}H_{13}N_2O_2^+$) and two fragments at m/z 236.5 and 210.7 corresponding to the loss of OH and CONH groups. Thus, the intermediate P7 was identified as monohydroxylated CBZ. The intermediate P6 with m/z 271.5 and three fragments at m/z 252.8, 236.5 and 209.9 corresponding to the consecutive loss of H_2O, OH and CONH groups were identified as dihydroxylated CBZ. Similar intermediates were also reported in previous literatures about the degradation of CBZ by
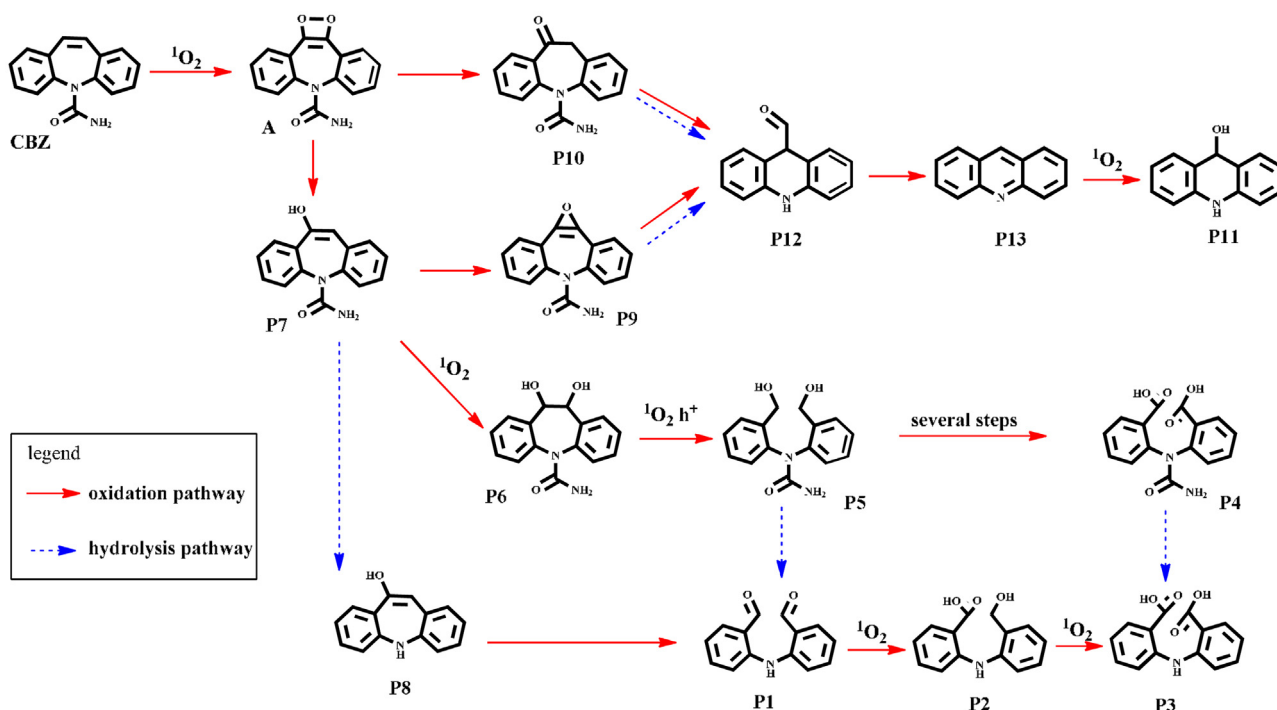
Fig. 12. Proposed oxidative degradation pathways of CBZ in the photocatalytic NBO system through hydroxylation reaction by $^1O_2$ and photogenerated h^+.

hydroxyl radicals and sulfate radicals in the advanced oxidation processes [30–34]. A possible mechanism was electrophilic attack at the olefinic double bond on the central heterocyclic ring of CBZ by hydroxyl radicals or sulfate radicals [31,33]. Intermediate P9 with m/z 251.4 was identified as 10,11-10,11-epoxycarbamazepine, which was formed through the dehydration of intermediate P7. Intermediate P5 was produced through the cleavage reaction of the azepine rings of intermediate P6 by photo-generated holes [33]. The complex hydroxylated intermediate (P4) was proposed to be produced from the further oxidation of P5 by the generated reactive species. Intermediate P10 was identified as quinine derivatives of intermediate P7, which was also found during the CBZ degradation by WO$_3$ photocatalytic oxidation [32] and by Mn(VII) and Fe(VI) [35]. The possible formation mechanism was that the addition reaction of singlet oxygen to the olefinic double bond on the central heterocyclic ring of CBZ molecular may lead to the formation of a dioxeten intermediate A, which was further transformed to compound P10 via a rearrange reaction.

In addition to the attack of photo-generated holes and $^1O_2$ on the middle carbon atom, the hydrolysis of the urea group on the central heteocyclic ring of CBZ was also invovled in the degradation and evolution of CBZ and its degradation intermediates. In this way, intermediates P1 and P8 were identified, which were generated from the hydrolysis of the urea group of intermediates P5 and P7. Then, intermediate P1 could be transormed to produce intermediates P2 and P3 through two steps of hydroxylation reaction.

Moreover, other two intermediates (P12 and P13) were identified by GC–MS as acridine-9-carboxaldehyde and acridine (Fig. S9). Similar intermediates were usually observed in the photo-induced degradation systems such as UV-radiation [36], UV/H$_2$O$_2$ [37] and BiPO$_4$ based photocatalytic systems [13]. Acridine-9-carboxaldehyde (P12) was formed from the facile ring contraction of intermediates P9 and P10 [37]. P12 was further converted to P13 via the cleavage of an aldehyde group, which suffered the oxidation by singlet oxygen to give P11 [36,37] (Fig. 12). Based on the above mentioned results, the oxidative degradation pathway of CBZ in the photocatalytic NBO system was proposed in Fig. 12.
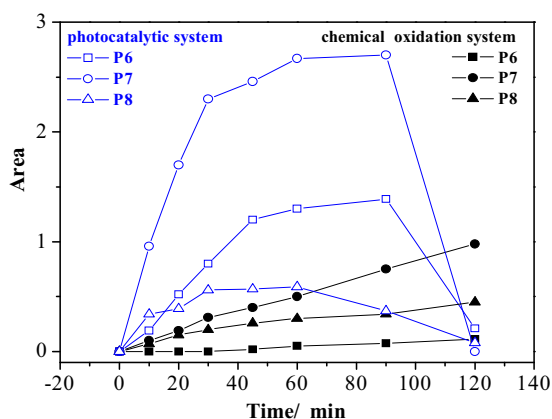

Fig. 13. Evolution of CBZ degradation intermediates in the photocatalytic and chemical oxidation degradation systems. The chemical structures of intermediates P6, P7 and P8 were shown in Fig. 12. Here, only the HPLC peak area of each intermediate was given to demonstrate its evolution.

Donner et al. observed that carbamazepine transformation products formed during UV photolysis were considerably more toxic than carbamazepine itself [38]. Therefore, the further degradation of CBZ degradation intermediates in the two concerned degradation systems was of importance to green oxidation of organic pollutants. Fig. 13 showed the generation, accumulation and further degradation of three main CBZ degradation intermediates (P6, P7 and P8) in the two degradation systems monitored by HPLC chromatograms. Due to the lack of authentic standards, the amount of degradation intermediates cannot be obtained. However, based on the peak area, the relative amount of degradation intermediates generated in the two systems can be compared. As shown in Fig. 13, three main CBZ degradation intermediates showed gradual increase in amount in 120 min in the chemical oxidation system. However, in the photocatalytic system, the three main CBZ degradation intermediates processed the similar evolution only in the initial 60 min, then they were rapidly decomposed

after 120 min. These results further confirmed the great advantage of dual reactive species for the degradation of CBZ in the photocatalytic oxidation system.

4. Conclusions

In the present work, we developed a facile chemical method for the preparation of metastable Bi^{3+} self doped $NaBiO_3$ (NBO) nanosheets by using acidic hydrolysis of $NaBiO_3$ in HNO_3 solutions. The as-prepared metastable Bi^{3+} self doped $NaBiO_3$ nanosheets showed both chemical oxidation ability and photocatalytic reactivity for the efficient degradation of CBZ. Under dark condition, $1.0\,g\,L^{-1}$ NBO nanosheets could degrade 57% CBZ ($20\,\mu mol\,L^{-1}$) in 60 min, while a nearly complete photodegradation of CBZ (99.8%) in 60 min was observed under the similar conditions. The illumination of visible light induced increased generation of singlet oxygen from the lattice oxygen of NBO by 2.2–3.8 times through photocorrosion. It is difficult to fully mineralize all the added CBZ by the single chemical oxidation, but the full mineralization of CBZ became possible by rapid decomposition of degradation intermediates in the photocatalytic system, which combined both the effects of the chemical oxidation and the intrinsic photocatalytic oxidation.

Acknowledgment

Appendix A. Supplementary data

Supplementary data associated with this article can be found, in the online version, at http://dx.doi.org/10.1016/j.apcatb.2016.09.054.

References

[1] M.A. Rogawski, Epilepsy Res. 68 (2006) 22–28.
[2] K. Stamatelatou, C. Frouda, M. Fountoulakis, P. Drillia, M. Kornaros, G. Lyberatos, Water Sci. Technol. 3 (2003) 131–137.
[3] M.J. Benotti, R.A. Trenholm, B.J. Vanderford, J.C. Holady, B.D. Stanford, S.A. Snyder, Environ. Sci. Technol. 43 (2009) 597–603.
[4] J. Drewes, T. Heberer, K. Reddersen, Water Sci. Technol. 46 (2002) 73–80.
[5] B. Halling-Sørensen, S.N. Nielsen, P. Lanzky, F. Ingerslev, H.H. Lützhøft, S. Jørgensen, Chemosphere 36 (1998) 357–393.
[6] S.D. Kim, J. Cho, I.S. Kim, B.J. Vanderford, S.A. Snyder, Water Res. 41 (2007) 1013–1021.
[7] T. Heberer, Toxicol. Lett. 131 (2002) 5–17.
[8] B.t. Ferrari, N. Paxéus, R.L. Giudice, A. Pollio, J. Garric, Ecotoxicol. Environ. Saf. 55 (2003) 359–370.
[9] I.K. Konstantinou, T.A. Albanis, Appl. Catal. B: Environ. 49 (2004) 1–14.
[10] J.C. Yu, J. Yu, W. Ho, Z. Jiang, L. Zhang, Chem. Mater. 14 (2002) 3808–3816.
[11] W. Zhao, W. Ma, C. Chen, J. Zhao, Z. Shuai, J. Am. Chem. Soc. 126 (2004) 4782–4783.
[12] X. Gao, X. Zhang, Y. Wang, S. Peng, B. Yue, C. Fan, Chem. Eng. J. 263 (2015) 419–426.
[13] J. Xu, L. Li, C. Guo, Y. Zhang, W. Meng, Appl. Catal. B: Environ. 130 (2013) 285–292.
[14] A.S. Prakash, C. Shivakumara, M.S. Hegde, L. Dupont, J.M. Tarascon, Mater. Res. Bull. 42 (2007) 707–712.
[15] A. Hameed, T. Montini, V. Gombac, P. Fornasiero, J. Am. Chem. Soc. 130 (2008) 9658–9659.
[16] D. Wu, L. Ye, S. Yue, B. Wang, W. Wang, H.Y. Yip, P.K. Wong, J. Phys. Chem.: C 120 (2016) 7715–7727.
[17] T. Zhang, Y. Ding, H. Tang, Chem. Eng. J. 264 (2015) 681–689.
[18] K. Yu, S. Yang, S.A. Boyd, H. Chen, C. Sun, J. Hazard. Mater. 197 (2011) 88–96.
[19] K. Yu, S. Yang, C. Liu, H. Chen, H. Li, C. Sun, S.A. Boyd, Environ. Sci. Technol. 46 (2012) 7318–7326.
[20] Y. Hu, D. Li, F. Sun, Y. Weng, S. You, Y. Shao, J. Hazard. Mater. 301 (2016) 362–370.
[21] W. Wang, X. Chen, G. Liu, Z. Shen, D. Xia, P.K. Wong, J.C. Yu, Appl. Catal. B: Environ. 176–177 (2015) 444–453.
[22] Y. Ding, X. Xia, Y. Ruan, H. Tang, Chemosphere 141 (2015) 80–86.
[23] Y. Ding, F. Yang, L. Zhu, N. Wang, H. Tang, Appl. Catal. B: Environ. 164 (2015) 151–158.
[24] M.A. Rubio, D.O. Mártire, S.E. Braslavsky, E.A. Lissi, J. Photochem. Photobiol. A: Chem. 66 (1992) 153–157.
[25] N. Serpone, I. Texier, A. Emeline, P. Pichat, H. Hidaka, J. Zhao, J. Photochem. Photobiol. A: Chem. 136 (2000) 145–155.
[26] Y. Nosaka, T. Daimon, A.Y. Nosaka, Y. Murakami, Phys. Chem. Chem. Phys. 6 (2004) 2917–2918.
[27] J.A. Rengifo-Herrera, K. Pierzchała, A. Sienkiewicz, L. Forrró, J. Kiwi, C. Pulgarin, Appl. Catal. B: Environ. 88 (2009) 398–406.
[28] P. Spathis, I. Poulios, Corros. Sci. 37 (1995) 673–680.
[29] C. Han, M.Q. Yang, B. Weng, Y.J. Xu, Phys. Chem. Chem. Phys. 16 (2014) 16891–16903.
[30] M.M. Ahmed, S. Chiron, Water Res. 48 (2014) 229–236.
[31] A. Ghauch, H. Baydoun, P. Dermesropian, Chem. Eng. J. 172 (2011) 18–27.
[32] Y.F. Rao, W. Chu, Y.R. Wang, Appl. Catal. A: Gen. 468 (2013) 240–249.
[33] Y.F. Rao, L. Qu, H. Yang, W. Chu, J. Hazard. Mater. 268 (2014) 23–32.
[34] J. Xu, L. Li, C. Guo, Y. Zhang, W. Meng, Appl. Catal. B: Environ. 130–131 (2013) 285–292.
[35] L. Hu, H.M. Martin, O. Arce-Bulted, M.N. Sugihara, K.A. Keating, T.J. Strathmann, Environ. Sci. Technol. 43 (2008) 509–515.
[36] T. Kosjek, H.R. Andersen, B. Kompare, A. Ledin, E. Heath, Environ. Sci. Technol. 43 (2009) 6256–6261.
[37] D. Vogna, R. Marotta, R. Andreozzi, A. Napolitano, M. d'Ischia, Chemosphere 54 (2004) 497–505.
[38] E. Donner, T. Kosjek, S. Qualmann, K.O. Kusk, E. Heath, D.M. Revitt, A. Ledin, H.R. Andersen, Sci. Total Environ. 443 (2013) 870–876.